LANGMUIR

pubs.acs.org/Langmuir Article

Unraveling the Phase Behavior and Stability of Surfactant-Free Microemulsions: From Molecular Interactions to Macroscopic Properties

Changsheng Chen, Yawen Gao, Mingbo Li,* and Chao Sun*

Cite This: https://doi.org/10.1021/acs.langmuir.4c03761 Read Online

ACCESS | Metrics & More | Article Recommendations | Supporting Information

ABSTRACT: Surfactant-free microemulsions (SFMEs), formed in mixed ternary systems such as water/ethanol/oil, have garnered substantial interest due to their unique properties and broad applications in areas such as enzyme-catalyzed reactions and nanoparticle synthesis. In this work, we conducted an in-depth investigation of the spontaneous nucleation and stabilization mechanisms of SFMEs, employing experimental techniques, molecular dynamics (MD) simulations, and Flory–Huggins (F–H) theory. The formation of multiscale nanostructures (characteristic scales of ∼1 and ∼100 nm) and their interfacial charging characteristics in SFMEs have been revealed experimentally. MD simulations investigated the structure and stability on the microscopic scale, enhancing our understanding of molecular interactions within these microemulsions. Our theoretical analysis revealed that the stability of mesoscopic nanodroplets within SFMEs hinges on a delicate balance between mixing entropy and internal energy. Equilibrium between these energies results in stable nanodroplet solutions, showcasing a delicate balance that can be manipulated by adjusting the volume fractions of the components and their interaction parameters. This research not only advances the theoretical understanding of SFMEs but also highlights their potential in industrial applications, emphasizing the importance of integrating theoretical and experimental approaches to develop functional nanostructured materials.

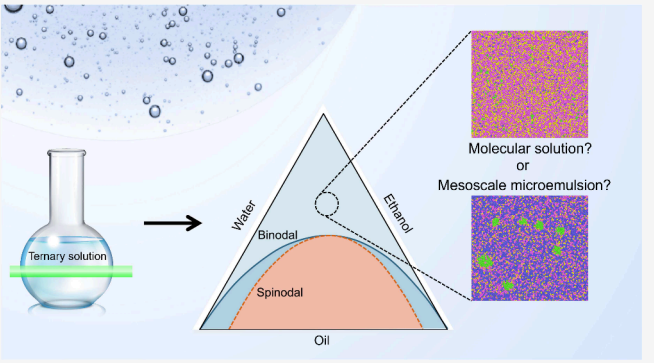

INTRODUCTION

Microemulsions, characterized as thermodynamically stable, isotropic, and transparent dispersions, are fascinating systems consisting of at least two immiscible fluids—typically a polar water phase and an apolar oil phase—stabilized by surfactants or amphiphilic compounds.[1−7] These surfactants possess a dual nature with hydrophilic heads and hydrophobic tails, allowing them to efficiently position themselves at the interface between oil and water phases.[7−9] Their strategic arrangement forms structured films that critically stabilize the microemulsion, leading to diverse morphologies such as oil-in-water (O/W), water-in-oil (W/O), and bicontinuous (BC) structures, corresponding to the Winsor I, II, and III types of classical Winsor classifications, respectively.[10]

Extensively documented in the literature, surfactant-based microemulsions (SBMEs) are well recognized for their versatility and applicability across a range of industrial and scientific processes. However, a less explored variant of these systems is the surfactant-free microemulsions (SFMEs), which emerge from ternary mixtures involving oil, water, and a hydrotrope (such as ethanol), typically.[11−15] Hydrotropes, differing from traditional surfactants, usually have smaller nonpolar tails and lack the ability to self-assemble into micelles or ordered films at the water/oil interface.[16,17] Instead, they improve the solubility of hydrophobic substances in aqueous solutions through the formation of dynamic clusters, leveraging hydrogen bonds with water molecules and showing strong functional similarities to cosolvents on both nano- and macroscales.[18]

To the best of our knowledge, SFME with W/O structure was first discovered in the ternary system of oil/water/n-propanol by Smith et al.[19] And they have been variously described in research as pre-ouzo phenomena,[20,21] detergentless microemulsions,[22,23] surfactant-free microemulsions (SFMEs),[24,25] or ultraflexible microemulsions (UFMEs),[26] highlighting their distinct nature and the broad scope of their theoretical and practical implications. Unlike SFMEs, kinetically frozen mesoscale microdroplets such as mesoscale solubilization[13,27−29] and micellar-like structural fluctuations[30]

Received: September 24, 2024
Revised: November 19, 2024
Accepted: November 19, 2024

have also been widely discussed and considered widespread. In addition, droplets in an oil−water two-phase system without ethanol also have recently attracted the attention of researchers due to their special properties.[31−33] Here, we follow most studies and use the term "SFME" to represent the first kind of thermodynamically stable nanostructures of a ternary system (oil/water/hydrotrope). The presence of these mesoscale structures, usually in the nanoscale range,[17,34−45] even has been confirmed as a general feature in water/hydrotrope mixtures containing hydrophobic organic substances.[15,16,27] These systems are intriguing not only for their unique formation mechanisms but also for their potential application in modern technology and medicine, such as facilitating enzymatic reactions, enhancing chemical reactions, synthesizing nanoparticles, improving drug delivery systems, and so on.[46−56] Despite their significant potential, the exploration of SFMEs remains limited, with studies on fewer than 20 systems documented.[15] This gap signifies a vast area ripe for research, particularly concerning their thermodynamic stability and the detailed molecular structure of these nanoentities, which are two key questions for SFME.

The recent proliferation of experimental techniques and molecular dynamics simulations has opened new avenues to probe the intricate microstructure and stabilization mechanisms of SFMEs.[21,57−60] These sophisticated approaches have started to shed light on the nuanced molecular interactions that govern the stability and microscopic behavior of SFMEs, suggesting that traditional theories like DLVO and binary Flory−Huggins might not fully capture the complexities involved in the spontaneous nucleation and stabilization of these systems.[21,57]

This work aims to build upon these findings, utilizing a combination of molecular dynamics simulations (MD), experiments, and theoretical analysis to elucidate the formation and stabilization mechanisms of SFMEs in general ternary systems. We extend our previous work[58,59] and present a theoretical model to expound on the spontaneous nucleation mechanism of SFME, setting the stage for a deeper understanding of these complex systems at the microlevel. This investigation not only contributes to the fundamental science underpinning SFMEs but also promises to expand the practical applications of these nanostructured fluids in various scientific and industrial scenarios.

MATERIALS AND METHODS

Chemicals and Sample Preparation. In this study, we investigated the formation of surfactant-free microemulsions using a ternary system comprising trans-anethol, ethanol, and water—components characteristic of the traditional beverage ouzo. trans-Anethol ($C_{10}H_{12}O$, molar mass: 148.2 g/mol, purity >99%) served as the oil phase and was purchased from Sigma-Aldrich, Germany. This component is commonly utilized in emulsion systems and was selected for its relevant physicochemical properties, including a dynamic viscosity of 2.34 mPa·s and a refractive index of 1.56, both measured at 25 °C. Ethanol, as a cosolvent, with a labeled purity of 99.9% was purchased from J&K Scientific (China). The ultrapure water with an electrical resistivity of 18.2 MΩ·cm and a natural pH of 6.54 was obtained via a Milli-Q water purification system (Merck, Germany).

The sample preparation was executed with precision and consistency. Initially, trans-anethol and ethanol were mixed until they were fully dissolved, followed by the gradual addition of water to achieve the desired volumetric ratios. Each mixture was prepared to a total volume of 50 mL and maintained at room temperature (25 °C). The compositions were defined by the volume fractions of the components: trans-anethol (ϕ_o), ethanol (ϕ_e), and water (ϕ_w), with the total sum of $\phi_o + \phi_e + \phi_w$ equating to 100%. Following the combination of the three constituents, the mixtures were subjected to gentle homogenization using a portable shaker for 3 min. This mild agitation was essential for the spontaneous formation of nanoscale structures, which remained uniformly dispersed throughout the solution.

Dynamic Light Scattering (DLS) Measurement. Dynamic light scattering (DLS) was employed to ascertain the size distribution of nano- or microstructurings within the ternary system using a ZEN3700 Zetasizer NanoZSE (Malvern, UK). The technique involved analyzing the correlation function curves of the aqueous phase. Measurements were conducted at a predetermined scattering angle of 173° using a quartz cuvette with a 10 mm optical path length. Each measurement required 1 mL of the prepared sample, which was introduced into the cuvette. Given that one of the components in the system was pure ethanol, which is prone to evaporation, the cuvette was hermetically sealed with a matched cap to prevent solvent loss at ambient temperature. Prior to each measurement session, the sample was allowed to equilibrate for 2 min to ensure uniform temperature distribution and stability at 25 °C. This preparatory step was crucial to maintaining consistent experimental conditions. To establish the reproducibility of our results, duplicate measurements were performed under identical conditions. For each measurement iteration, a series of six individual tests were carried out to calculate the average size distribution of the emulsions. There was a brief pause of 10 s after each test to ensure accuracy and consistency in the readings. The total scattering intensity of light (TSIR, in kilocounts per second) was recorded for each microentity within the emulsion. This data were then processed through photon counting, further adjusted by an attenuator. For a comprehensive understanding of the DLS measurement principles utilized in this study, readers are referred to previous work,[58] which details the methodological framework and theoretical underpinnings.

Zeta Potential Measurement. The zeta potential of the nanoscale structures within the microemulsions was evaluated using the same DLS apparatus but with a specific module designed for zeta potential measurement. The measurement of this parameter was performed under controlled environmental conditions (25 °C), following the equilibration protocols established for the size distribution analysis to ensure consistency in the experimental setup. The U-shaped capillary cuvettes (filled with 1 mL of sample) were used to perform the measurements with automated runs. The zeta potential was calculated according to the Smoluchowski model. For each sample tested, the measurement was repeated six times with a 10 s delay between them.

Nanoparticle Tracking Analysis (NTA) Measurement. Nanoparticle tracking analysis (NTA) technology determines particle size by tracking and analyzing the trajectories described by individual particles in the suspension. Moreover, it can image the particles directly so that their number concentration can be easily obtained. Here a home-built NTA system, consisting of an optical dark-field microscope equipped with a high-speed camera, a laser, and a glass sample cell, was applied. A finely focused laser beam (wavelength of 520 nm) is refracted twice by a prism-edged optical flat and enters the sample microchamber with a height of 500 μm. The visible area covered by the laser beam is about 440 μm × 200 μm. For more details on the NTA system, please refer to our previous work.[61]

MD Simulations. The molecular dynamics (MD) simulations were performed to study the microstructure and stabilization mechanisms of SFME within a universal ternary system composed of water/ethanol/oil, using the large-scale atomic/molecular massively parallel simulator (LAMMPS) package.[62] The simulation model comprised Lennard-Jones (LJ) particles representing water (W), ethanol molecules, oil (O, analogous to trans-anethol), and solid surfaces (S). To streamline the model for computational efficiency, each molecule segment was represented by a single LJ bead: H_2O, CH_2 (or CH_3), and OH, as depicted in Figure 1(a). This representation allowed for the adjustment of interaction parameters between LJ beads to accurately reflect the intrinsic properties of water,

https://doi.org/10.1021/acs.langmuir.4c03761
Langmuir XXXX, XXX, XXX−XXX

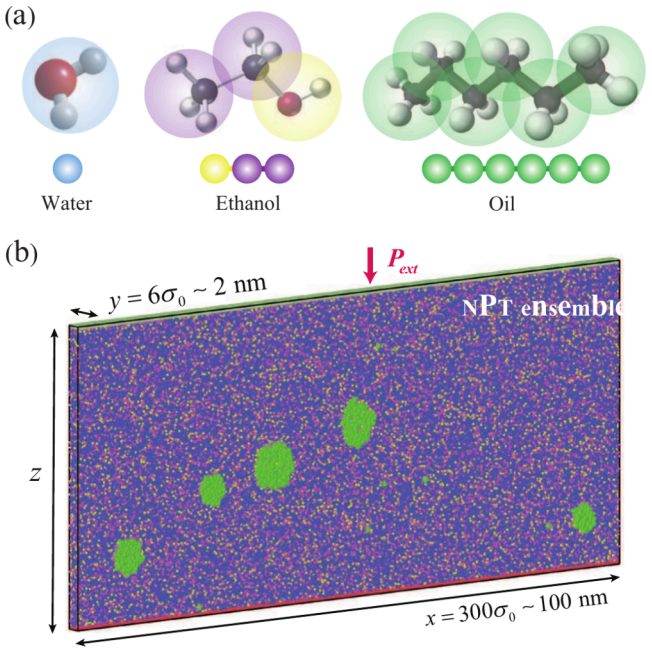

Figure 1. (a) Optimized structures and coarse-graining schemes of water, ethanol, and oil molecules. (b) The ensemble diagram and the 2D box size diagram of MD simulation.

ethanol, and oil. Furthermore, a coarse-grained, chain-like model was employed for both ethanol and oil molecules. The ethanol molecule was modeled with one hydrophilic head (H) bead and two hydrophobic tail (T) beads, while the oil molecule was represented by six identical hydrophobic beads. This simplified molecular representation aids in elucidating the fundamental interactions and structural dynamics of each component in a microemulsion at the microlevel.

The nonbonded interaction $U_{ij}(r)$ between any two beads i and j is represented by either the Lennard-Jones (LJ) potential or the Weeks−Chandler−Andersen (WCA) potential, both of which can be given by

$$U_{ij} = 4\epsilon_{ij}\left(\left[\left(\frac{\sigma_{ij}}{r}\right)^{12} - \left(\frac{\sigma_{ij}}{r}\right)^{6}\right] - \left[\left(\frac{\sigma_{ij}}{r_c}\right)^{12} - \left(\frac{\sigma_{ij}}{r_c}\right)^{6}\right]\right), \quad r < r_c \tag{1}$$

where r is the distance between the particles, r_c is the truncated distance, σ_{ij} is the size parameter, and ϵ_{ij} is the energy parameter. Different from the standard LJ potential, the WCA potential is purely repulsive and was used here to represent the unfavorable interaction. In the LJ potential, the cutoff distance r_c was set to $3.2\sigma_0$, while for the WCA potential, $r_c = 2^{1/6}\sigma_0$. All variables, unless specified, are presented in reduced units with length and energy scales set by the LJ parameters of the solvent−solvent interaction (hereafter denoted as σ_0 and ϵ_0, respectively). The interaction parameters used are given in the Supporting Information (Table S1). To convert the reduced units to actual units, the solvent particles can be considered to be argon atoms. The bonded intramolecular interactions of the ethanol molecules and oil molecules are modeled using a finite extensible nonlinear elastic (FENE) potential,[63] $U_{FENE}(r) = -\frac{1}{2}kr_0^2\left[1 - \left(\frac{r}{r_0}\right)^{12}\right]$, where r is the bond length. The maximum bond length was set to $r_0 = 1.5\sigma_0$, and the spring constant was set to $k = 30\epsilon_0\sigma_0^{-2}$.

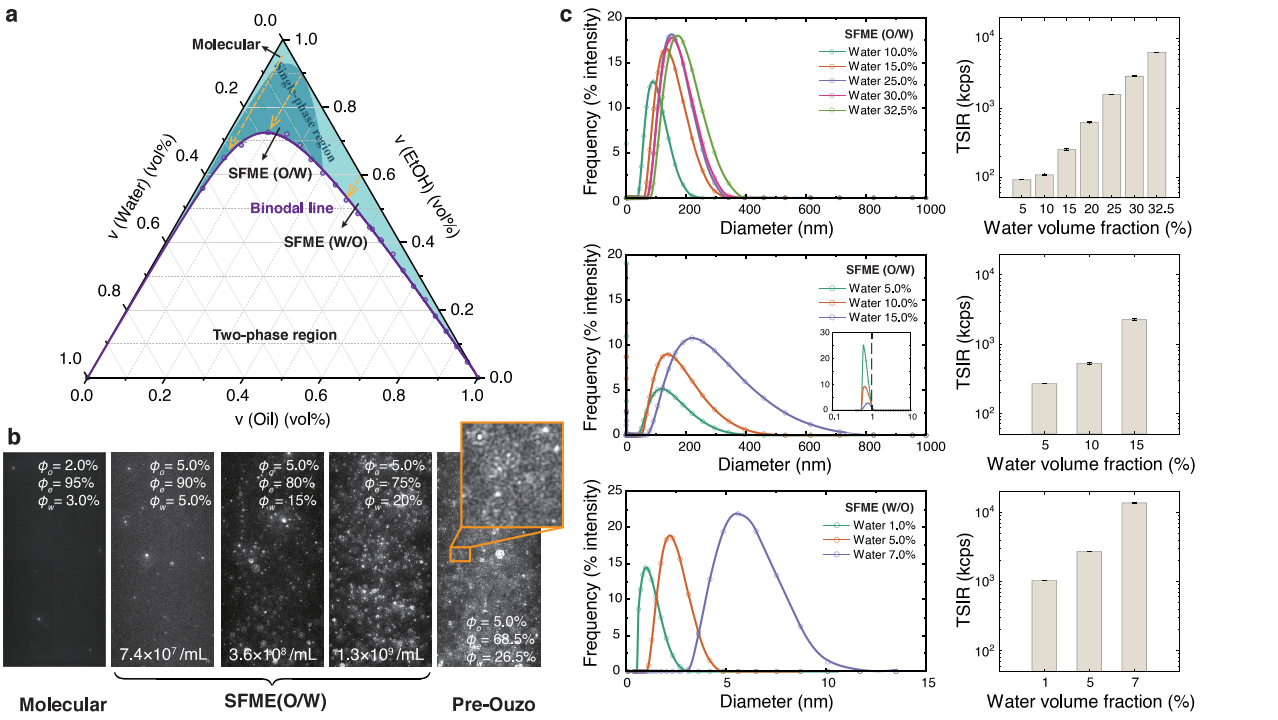

Figure 2. (a) Ternary phase diagram of oil(trans-anethol)/ethanol/water systems under ambient conditions (25 °C). All concentrations are in volume fractions. The smooth line across the points is the binodal line. The colored area is the single and homogeneous region, which contains the molecular solution, the SFME (O/W), and the reverse-SFME (W/O). The white area corresponds to the multiphasic region. (b) Microscopic images from the NTA experiments, showing the evolution of microstructures captured along a path that gradually approaches the binodal line (from left to right). (c) Size distribution of the mesoscale inhomogeneities observed in the single-phase domain of the ternary phase diagram. The data is shown along three different paths at constant oil volume fraction (top: 2.5%, middle: 10%, bottom: 40%) and varying water volume fractions (as shown by the yellow arrow in (a)). The right column correspondingly presents the dependence of the total scattering intensity rate of the mesoscale inhomogeneities (count rate, kcps) on the water volume fraction.

https://doi.org/10.1021/acs.langmuir.4c03761
Langmuir XXXX, XXX, XXX−XXX

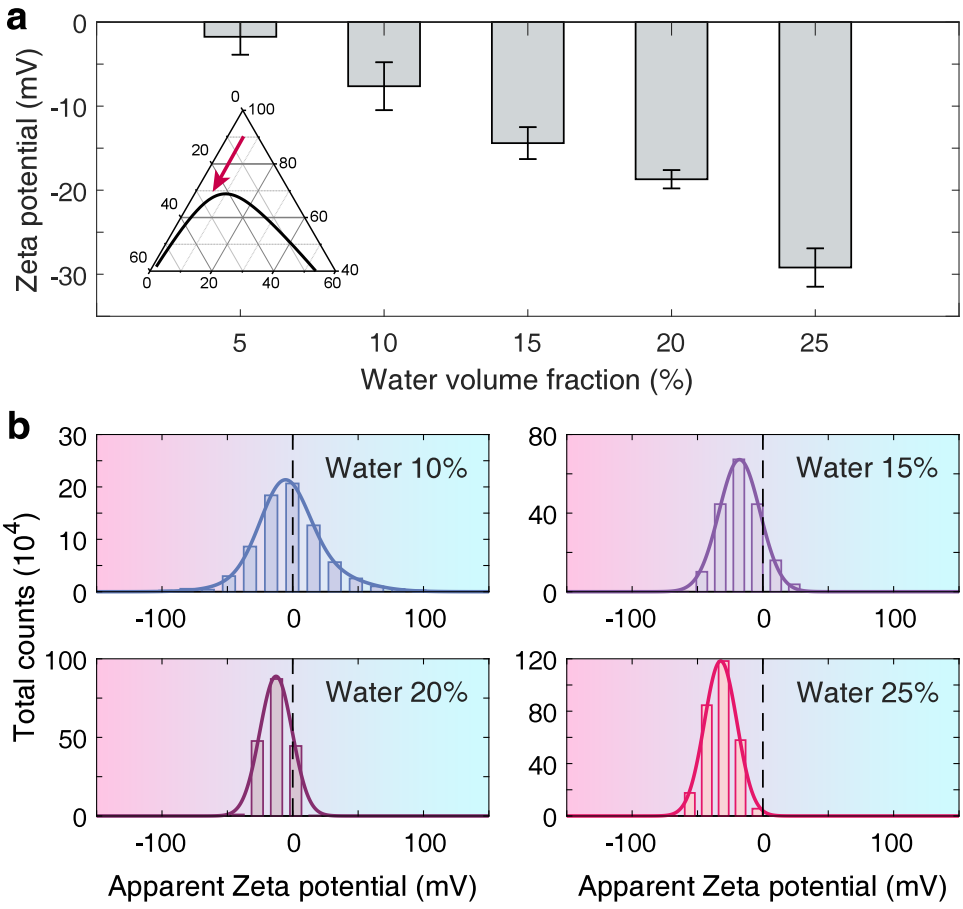

Figure 3. Zeta potential measurements. (a) Global zeta potential of SFME (O/W) for various ternary solutions with compositions in the single-phase region. The inset shows the data obtained along this path. (b) Distribution of zeta potential in the mesoscopic droplet population for various ternary solutions.

Isothermal and isobaric (NPT) simulations were conducted on the system comprising water, ethanol (acting as a hydrotrope), and oil. Note that in our coarse-grained simulation, we chose 6 beads (segments) of oil instead of 10 beads of trans-anethol to save computer losses for simulation, as the computer losses will increase rapidly with increasing chain length. For these simulations, a quasi-two-dimensional (2D) simulation box was employed, measuring 900 × 6 × z in units of σ_0, as depicted in Figure 1(b). To delineate the boundaries of the simulation environment, two smooth solid substrates composed of frozen solid atoms were positioned at the top and bottom of the box. Periodic boundary conditions were applied along the x and y axes to mimic an infinite system. The dynamics within the simulation were governed by integrating the equations of motion using the classic velocity-Verlet algorithm, with an integration time step of 0.0023τ, where $\tau = \sqrt{m_0/\epsilon_0}$ represents the characteristic time scale and m_0 is the mass of the solvent atom. The system temperature T was strictly maintained at $k_BT = 0.846\epsilon_0$, with k_B denoting the Boltzmann constant. Temperature regulation was achieved using a Nose-Hoover thermostat, which was configured with a time constant of 0.23τ, ensuring thermal equilibrium throughout the simulation.

The simulations were conducted as follows. The simulation box, bounded by two solid substrates, was initially populated with 216,000 fluid beads. These beads represented a mixture of water molecules (n_w), ethanol molecules (n_e), and oil molecules (n_o), distributed randomly throughout the volume. Given that the volume v_m of each bead is a constant and approximates to σ_0^3, the volume fractions of oil, water, and ethanol can be respectively expressed as

$$\phi_w = \frac{n_w}{n_t},\ \phi_e = \frac{3n_e}{n_t},\ \phi_o = \frac{6n_o}{n_t} \tag{2}$$

where the total number of beads is $n_t = 216000 = n_w + 3n_e + 6n_o$. The simulation parameters (Table S1) were meticulously adjusted to explore different scenarios by varying the volume fractions ϕ_w, ϕ_e, and ϕ_o. This adjustment was achieved by controlling the quantities of molecules n_w, n_e, and n_o. A comprehensive 200 ns NPT simulation run was performed to attain the final phase equilibrium and assess the miscibility of the three components. The external pressure was set to $P_{ext} = 0.0122\epsilon_0\sigma_0^{-3}$. Based on the interaction parameters between different components, it was possible to achieve complete solubility between water and ethanol, as well as between ethanol and oil, under specific conditions. However, the solubility between oil and water remained elusive, as these components are typically immiscible. By strategically manipulating the ratios of ϕ_w, ϕ_e, and ϕ_o, the simulations were designed to emulate various physicochemical phenomena.

RESULTS AND DISCUSSION

Formation of Multiscale Nanostructures. In the traditional ouzo emulsion system, trans-anethol, serving as the oil phase, demonstrates immiscibility with water while maintaining solubility in ethanol. This ternary composition exhibits intricate phase behaviors, ultimately culminating in the formation of a comprehensive ternary phase diagram, as illustrated in Figure 2(a). The overall diagram is partitioned by a binodal line that demarcates the distinction between the single- and two-phase regions, derived empirically from a series of experimental data points.

https://doi.org/10.1021/acs.langmuir.4c03761
Langmuir XXXX, XXX, XXX−XXX

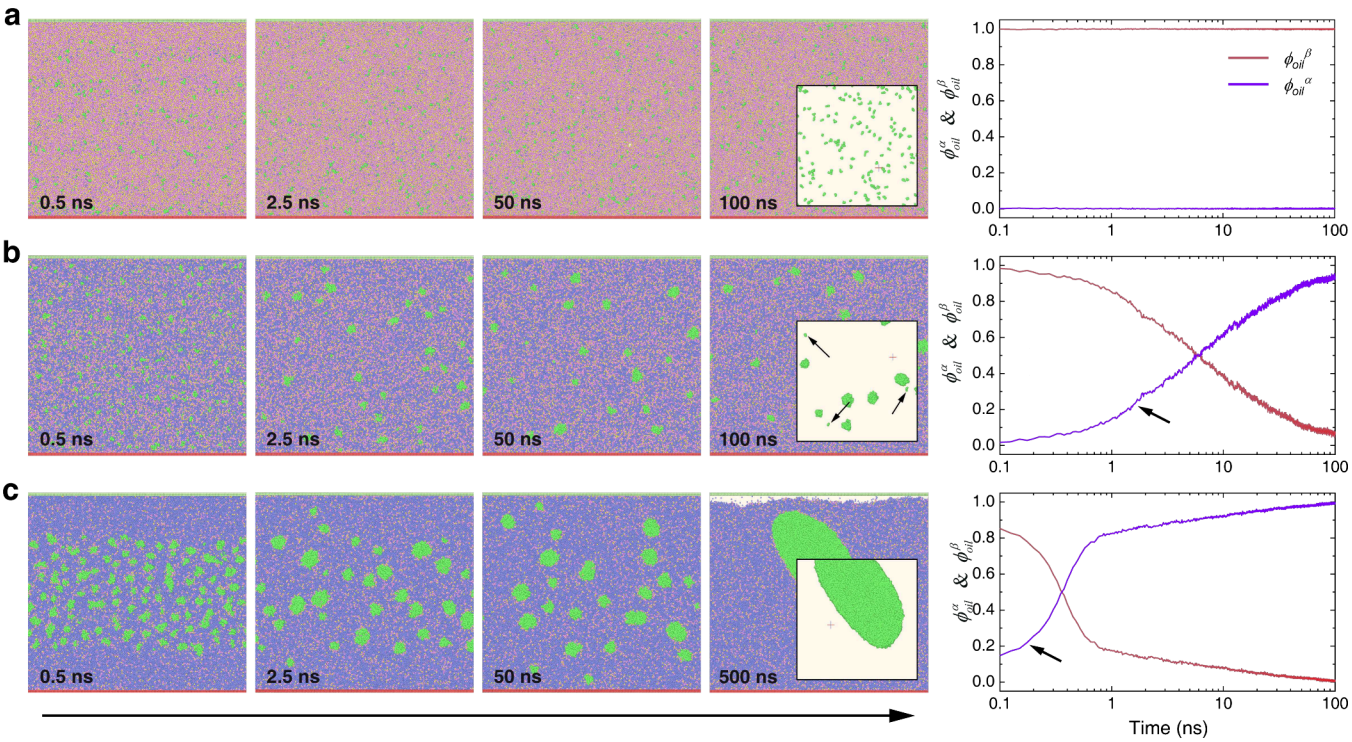

Figure 4. MD simulation snapshots under three different systems. (a) System A (ϕ_w = 0.025, ϕ_e = 0.95, ϕ_o = 0.025) ultimately forms a homogeneous molecular solution after running for 100 ns. (b) System B (ϕ_w = 0.45, ϕ_e = 0.5, ϕ_o = 0.05) eventually forms stable nanodroplets after running for 100 ns. (c) System C (ϕ_w = 0.6, ϕ_e = 0.25, ϕ_o = 0.15) eventually forms large liquid droplets, similar to phase separation. For the convenience of viewing oil molecules (green), ethanol and water molecules are hidden in the inset. The width of each subsnapshot in (a−c) is 46 nm. The three plots in the right column show the distribution of oil molecules in the oil droplets phase (α phase) and the mixed solution phase around oil droplets (β phase) as a function of time for the three systems, respectively. Here $\phi_{oil}^{\alpha} = n_{oil}^{\alpha}/n_{oil}^{tot}$, $\phi_{oil}^{\beta} = n_{oil}^{\beta}/n_{oil}^{tot}$, where n_{oil}^{α} represents the number of oil molecules in the α phase, n_{oil}^{β} represents the number of oil molecules in the β phase, and n_{oil}^{tot} represents the total number of oil molecules in two phases. The arrows in statistical plots indicate the beginning of nucleation.

Within the single-phase domain, the mixture displays a variety of nanostructures, ranging from homogeneous molecular solutions to mesoscale nanostructures and reverse aggregates, as shown in Figure 2(b). The manifestation of these structures is contingent upon the volumetric proportions of the constituent components. Within the molecular-solution region, the system exhibits no well-defined structures in the view. As the composition of ternary solution approaches the phase boundary, more mesoscopic droplets nucleate and their concentration increases exponentially with the proportion of water component. The rightmost snapshot is taken at a point very close to the phase boundary but still within the single-phase SFME (O/W) domain. Under these conditions, the system is in a metastable thermodynamic state, in which discrete SFME droplets and concentration fluctuations merge, making them difficult to differentiate. This observation suggests that phase separation is likely to occur between two phases that share similar correlation lengths.

This ternary system is characterized by two distinct types of SFMEs—SFME (O/W) and SFME (W/O)—which are identifiable based on the size of the suspended nanoscale structures. Figure 2(c) displays the size distribution of these identifiable nanostructures (left column) alongside the corresponding total scattering intensity rate (TSIR, right column) across various compositions. These measurements were conducted along paths at constant oil volume fractions while varying water volume fractions, gradually approaching the miscibility limit, as indicated by the dotted arrows on the phase diagram (Figure 2(a)). In the SFME region, with a low volume fraction of the oil component, only mesoscopic droplets of approximately 100 nm are formed (top panel). The size distribution range then progressively shifts rightward with the increase in the water component's volume ratio. With a further increase in the oil component's volume ratio, two types of nanostructures emerge (middle panel): molecular-scale oil aggregates (approximately 1 nm) and mesoscale droplets (approximately 100 nm). Approaching the demixing boundary, the concentration of these smaller aggregates diminishes and eventually vanishes (see the inset), while more substantial and larger mesoscopic droplets are generated, expanding the size distribution to approximately 800 nm. In the reverse-SFME region, where the water component is dispersed, sizes reduce to just a few nanometers (bottom panel). Near the miscible boundary, the size of these water-enriched aggregates, with well-defined interfaces, grows to about 7 nm, highlighting a complete transformation in the structure of the interfacial molecular arrangement between SFME (O/W) and reverse-SFME (W/O). Correspondingly, the TSIR for these multiscale nanodomains, depicted in the right column, reflects global scattering information from a spatially uniform flow field. The scattering intensity increases exponentially and spans 2 orders of magnitude on the absolute scale with the rising water volume fraction, confirming that near the boundary, these nanostructures increase not only in size but also in their number concentration.

We then explored the colloidal stability of these SFMEs by assessing their zeta potential distribution, as illustrated in Figure 3. Here, the mean diameter of the mesoscopic droplets

https://doi.org/10.1021/acs.langmuir.4c03761
Langmuir XXXX, XXX, XXX−XXX

is approximately 200−300 nm at different water volume fractions.[58] To enhance the precision of our zeta potential measurements, we meticulously calibrated several parameters, including the viscosity, refractive index, and dielectric constant, across varying compositions of the ternary solution (see Figure S1 in the Supporting Information).

The overarching zeta potentials of SFMEs were analyzed for compositions progressively nearing the phase-separation boundary, as depicted in the inset of Figure 3(a). This analysis entailed maintaining a constant fraction of oil while incrementally increasing the water component fraction. We observed that the SFME (O/W) mesoscopic droplets generally exhibit a macroscopic negative charge. Notably, as the composition approaches the phase boundary, the magnitude of the zeta potential escalates, suggesting a higher colloid stability. Interestingly, a more detailed microscopic examination of the zeta potential distribution within this SFME (O/W) droplet population revealed that not all mesoscopic droplets uniformly carry a negative charge. As depicted in Figure 3(b), a subset of these mesoscopic droplet populations also manifests positive charges at their interfaces, particularly in compositions far from the phase boundary. Unraveling the underlying mechanisms responsible for this charge distribution and its implications for SFME stability and behavior is a compelling subject for our future study.

Spontaneous Nucleation and Molecular Structure. Experimental observations have confirmed the stable existence of multiscale nanostructures within surfactant-free microemulsion systems (SFMEs), raising pertinent questions regarding (1) the driving mechanisms behind the spontaneous nucleation of SFMEs and (2) the molecular arrangements at interfaces. To elucidate these nanostructural details at the molecular level, molecular dynamics (MD) simulations were conducted across a range of compositional systems, each distinguished by specific volume fractions of their components. It is crucial to acknowledge that the purpose of these simulations was not to replicate the experimental systems entirely but rather to generalize the properties of such three-component solutions by constructing a more general ternary system.

Here we examined three distinct compositions aligned with different regions of the phase diagram, as detailed in Figure 4. System A (Sys. A) consisted of three components: oil, ethanol, and water, with respective volume fractions of $\phi_o = 0.025$, $\phi_e = 0.95$, and $\phi_w = 0.025$. Notably, the high concentration of ethanol, a hydrotrope, facilitated the complete dissolution of oil molecules over a simulation period of 100 ns, leading to a homogeneous molecular solution without the nucleation of discernible nanostructures (Figure 4(a)). This simulation outcome aligns with the experimental findings of molecular solution observed in Figure 2(b), in which there is no nucleation of any nanostructure that can be called a droplet.

Conversely, upon reducing the ethanol proportion and increasing the water fractions, System B (Sys. B), with a composition of $\phi_o = 0.05$, $\phi_e = 0.50$, and $\phi_w = 0.45$, displayed the spontaneous nucleation and stabilization of nanodroplets within a size range of 3 to 8 nm over the simulation period, as shown in Figure 4(b). Typically, after about 100 ns, the system has reached a steady state and the size of these nanodroplets no longer changes. This configuration supports the experimental observations of SFMEs (Figure 2) and underscores our MD simulations' capability to capture the essential characteristics of such ternary systems. Notably, a minor proportion of oil molecules remained in the continuous phase (see the inset), indicating that the insoluble oil achieves a coexisting state between the nanodroplet and solution phases. This highlights the dynamic stability and variability of the droplets within this system. This actually explains why we found multiscale nanodomains, i.e., molecular-scale oil aggregates (∼1 nm) and mesoscale droplets (∼100 nm), in our experimental results.

Further adjustments to the component ratios in System C (Sys. C), which increased the volume fractions of oil and water and decreased the ethanol proportion ($\phi_o = 0.15$, $\phi_e = 0.25$, and $\phi_w = 0.6$), led to rapid nucleation of multiple small droplets (∼0.5 ns) and the eventual stabilization of a single large droplet (∼500 ns) in the bulk, as depicted in Figure 4(c). Interestingly, the oil molecules in this case are confined entirely to the sole droplet (pure oil phase) with almost no oil molecules in the continuous phase. Given the limitations of the MD simulation scale, the droplets in Sys. C, although nanoscale, suggest a potential to appear at the macroscale when extrapolated to macroscopic dimensions. This result suggested a potential for macroscopic manifestations of these nanoscale droplets, leading to a turbid solution or complete phase separation, akin to the multiphase region and the ouzo phenomenon.

The findings presented herein elucidate that the spontaneous nucleation of oil droplets in Sys. B and Sys. C can occur. We explore these phenomena further by applying the classical nucleation theory. Theoretical calculations reveal that the nucleation energy barrier ΔG^* for Sys. B is $7.24k_BT$, while for Sys. C, it is substantially lower at $0.14k_BT$ (for detailed calculations, see the Supporting Information). Both values are below the critical threshold of $\sim 10k_BT$, indicating the propensity for spontaneous nucleation in these systems. Conversely, in Sys. A, the free energy ΔG increases monotonically with the radius r of the oil droplet, showing no maximum point, which signifies a lack of conditions favorable for spontaneous nucleation. The nucleation rate equation $J = J_0 \exp(-\Delta G^*/k_BT)$, where J_0 is the pre-exponential factor, also supports these findings. Sys. C, with its notably lower energy barrier, exhibits a significantly faster nucleation rate, corroborated by MD simulation results indicating nucleation events at 0.25 and 2.5 ns for Sys. C and Sys. B, respectively, as observed in Figure 4 (indicated by the arrow in the right column).

Additionally, Sys. B is characterized by the formation of multiple small-scale nanodroplets that exhibit prolonged stability, typifying the stable nanodroplet solutions observed in SFMEs. The experimentally observed droplet sizes, ranging from several nanometers up to 100 nm (Figure 2(c)), provoke further investigation into the microstructural characteristics of these nanodroplets. Our simulations replicate the presence and microstructures of these SFMEs effectively. Figure 5 illustrates the distribution of ethanol, water, and oil molecules along the radial direction r of the droplets in Sys. B and Sys. C, showing a significant enrichment of ethanol at the droplet interfaces. As an amphipathic molecule, this enrichment substantially lowers the interfacial tension between the nanodroplets and the surrounding solution, enhancing droplets' stability.

These observations lend strong support to the hypothesis that nanostructured environments within SFMEs can coexist seamlessly with the solution phase, facilitated by the intricate molecular configuration and dynamic interactions within the system. Notably, statistical analysis reveals that the concen-

https://doi.org/10.1021/acs.langmuir.4c03761
Langmuir XXXX, XXX, XXX−XXX

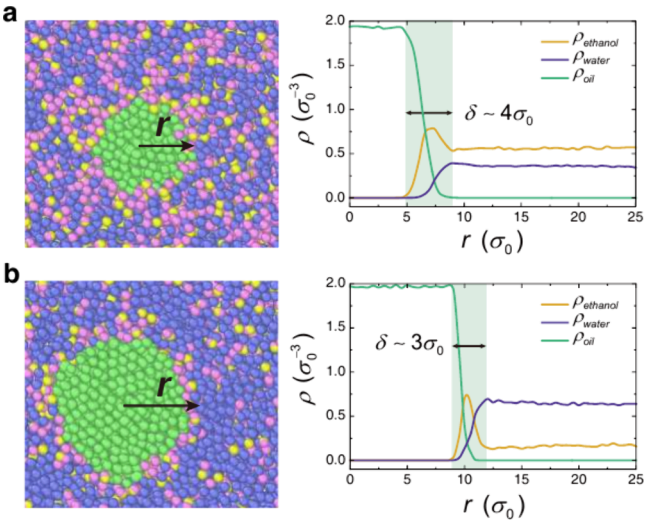

Figure 5. (a) and (b) show that the distribution of ethanol molecules, water molecules, and oil molecules along the radius of the droplet toward the outside for Sys. B and Sys. C, respectively. The left column shows local snapshots of a droplet in the MD simulations of Sys. B and Sys. C. The right column shows the statistical distribution of density ρ along the radial r direction of droplets in Sys. B and Sys. C.

tration of ethanol at the droplet interfaces is higher and the interfacial layer is thicker in Sys. B than in Sys. C (right column in Figure 5). This phenomenon may explain why smaller droplets in Sys. B are more stable; typically, smaller droplets experience higher Laplace pressures ($\Delta p = \gamma/r$ in a 2D system, where γ is the interfacial tension), which generally pose challenges to stability. This comprehensive analysis underscores the intricate balance of molecular interactions that govern the stability and behavior of nanodroplets in SFME systems.

Stabilization Mechanism. In our simulation system, ethanol and oil are modeled as chain-like molecules comprising multiple beads, reminiscent of short-chain polymers. This structural similarity prompted us to consider the Flory–Huggins (F–H) theory, traditionally applied to polymer solutions, as a theoretical framework to analyze the phase behavior of the oil/ethanol/water system.[64−66] The F–H theory provides a quantitative description of the mixing and phase separation behavior in binary solutions. For a binary mixture composed of components a and b, the F–H free-energy density can be expressed as follows

$$f(\phi_a, \phi_b) = \frac{\Delta F_{mix}}{n_t k_B T} = \frac{\phi_a}{N_a} \ln \phi_a + \frac{\phi_b}{N_b} \ln \phi_b + \chi_{ab} \phi_a \phi_b \tag{3}$$

where f represents the free-energy density, N_a denotes the number of segments in a molecule of type a, ϕ_a is the volume fraction of component a, and $\phi_b = 1 - \phi_a$ represents the volume fraction of component b. The interaction parameter, χ_{ab}, is given by $\chi_{ab} = -z(\epsilon_{aa} + \epsilon_{bb} - 2\epsilon_{ab})/2k_BT$, where z is the coordination number, and the interaction energy between molecules i and j, ϵ_{ij}, can be obtained from the MD simulations. The first two terms quantify the contribution from mixing entropy, illustrating how randomness in the system increases with mixing. The last term accounts for the average internal energy arising from interactions between components a and b. By applying eq 3, we can derive the free-energy curves for the system, facilitating the determination of critical points, such as binodal and spinodal lines, where phase separation occurs.

For ternary systems, F–H theory can be extended by certain methods.[67−71] The free-energy density for a ternary system is given as

$$f(\phi_a, \phi_b, \phi_c) = \frac{\Delta F_{mix}}{n_t k_B T} = \frac{\phi_a}{N_a} \ln \phi_a + \frac{\phi_b}{N_b} \ln \phi_b + \frac{\phi_c}{N_c} \ln \phi_c + \chi_{ab} \phi_a \phi_b + \chi_{bc} \phi_b \phi + \chi_{ac} \phi_a \phi_c \tag{4}$$

where χ_{ij} is the Flory–Huggins interaction parameter between components i and j. The values χ_{ab}, χ_{bc}, and χ_{ac} can be obtained by referring to the definition in eq 3 and the value of ϵ_{ij} in Table S1, i.e., $\chi_{we} = -0.273$, $\chi_{wo} = 2.056$, and $\chi_{eo} = -0.507$. Note that in eq 4 we have omitted some of the linear terms for ϕ_a, ϕ_b, and ϕ_c for computational convenience. The omission of these linear terms does not affect the results of phase separation due to the quadratic derivative.[67] Meanwhile, to simplify the calculations, ternary interaction coefficient χ_{abc} is assumed to be zero and therefore is ignored.[69,72]

Although obtaining phase diagrams for ternary solutions is more complicated than that for binary systems, it is possible to calculate phase diagrams based on this simplified theoretical model. If the volume fractions ϕ_b and ϕ_c are chosen as the independent composition variables, where $\phi_a = 1 - \phi_b - \phi_c$, then the second derivative of the free energy f can be written as[67−69]

$$D = \det\left(\frac{\partial^2 f}{\partial \phi_b \partial \phi_c}\right) = \left(\frac{\partial^2 f}{\partial \phi_b^2}\right)_{n_t, \phi_c} \left(\frac{\partial^2 f}{\partial \phi_c^2}\right)_{n_t, \phi_b} - \left[\left(\frac{\partial^2 f}{\partial \phi_b \partial \phi_c}\right)_{n_t}\right]^2 \tag{5}$$

The spinodal line, i.e., boundary condition between the stable region and the unstable region, is where D vanishes. Substituting the expressions for the derivatives $\partial^2 f/(\partial \phi_a \partial \phi_b)$ into the spinodal constraint $D = 0$, eq 5 can convert into the relationship

$$\left(\frac{1}{N_b \phi_b} + \frac{1}{1 - \phi_b - \phi_c} - 2\chi_{ab}\right) \times \left(\frac{1}{N_c \phi_c} + \frac{1}{1 - \phi_b - \phi_c} - 2\chi_{ac}\right) - \left(\frac{1}{1 - \phi_b + \phi_c} + \chi_{bc} - \chi_{ab} - \chi_{ac}\right)^2 = 0 \tag{6}$$

Additionally, the binodal curve, also called the miscibility gap, could be calculated based on the below chemical potential equilibrium[67,69,71]

$$\mu_i^{\alpha} = \mu_i^{\beta} \ (i = a, b, c) \tag{7}$$

where α and β indicate two different phases, i.e., oil droplet phase and surrounding aqueous phase. The chemical potential of component i, i.e., the partial molar amount of Gibbs free energy, can be expressed as[67]

$$\mu_i = \frac{\partial G}{\partial N_i} = \frac{\partial [pV + n_t k_B T f(\phi_i)]}{\partial N_i} = p v_m + k_B T f(\phi_i) + n_t k_B T \frac{\partial f}{\partial \phi_i} \tag{8}$$

where v_m is the volume of a single bead (segment), V is the total volume, and p is the pressure of the system.

https://doi.org/10.1021/acs.langmuir.4c03761
Langmuir XXXX, XXX, XXX−XXX

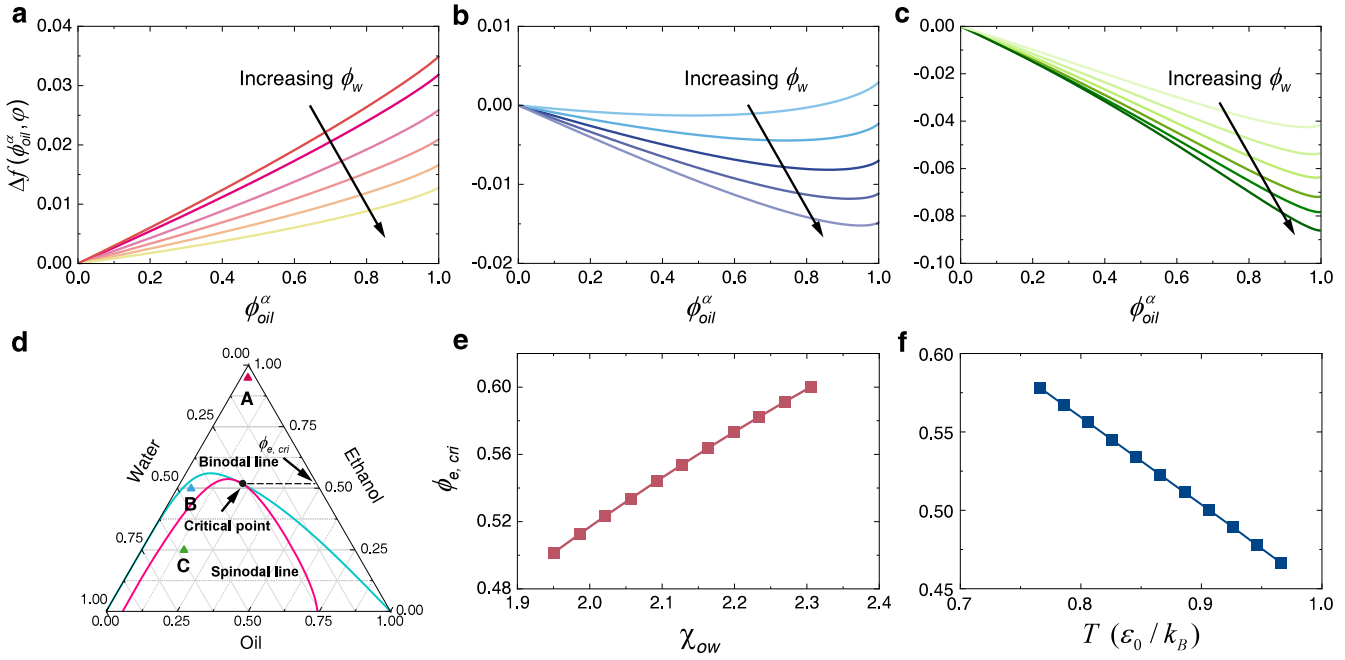

Figure 6. (a−c) The free-energy density curves of systems A, B, and C were calculated through eq 4. The different free energy f curves with various color represent different fractions ϕ_a. ϕ_a increases along the direction of the arrow. (d) Phase diagram of the water/ethanol/oil ternary system was calculated from eq 4 and eq 6. Sys. A, Sys. B, and Sys. C correspond to the monophasic zone (homogeneous molecular solutions), transition zone (mesoscopic nanodroplets), and multiphase zone (phase separation), respectively. The red line represents the spinodal line, and the cyan line, the binodal line. The intersection of the two donates the critical point. (e) The position of critical point $\phi_{e,cri}$ varies with the interaction parameter between oil and water χ_{ow}. (f) The position of critical point $\phi_{e,cri}$ varies with the temperature T.

Utilizing eq 4, we calculated the free-energy density $f(\phi_{oil}^{\alpha}, \phi_i)$ as a function of ϕ_{oil}^{α} for Systems A, B, and C. The results of these calculations are depicted in Figure 6(a−c). The interaction parameter χ_{ij}, critical for these calculations, was determined using the MD simulation parameters listed in Table S1. Within these figures, ϕ_{oil}^{α} quantifies the fraction of oil molecules in the droplet phase (α phase) relative to the total number of oil molecules, formulated as $\phi_{oil}^{\alpha} = n_{oil}^{\alpha}/n_{oil}^{tot}$. Therefore, a ϕ_{oil}^{α} value of 0 implies that all oil molecules are dispersed within the solution, indicating the absence of any droplets. Conversely, $\phi_{oil}^{\alpha} = 1$ suggests that all oil molecules are sequestered within the droplet phase, with none remaining in the surrounding mixing solution phase (β phase). Intermediate values, $0 < \phi_{oil}^{\alpha} < 1$, denote a distribution of oil molecules across both the droplet and continuous phases.

According to the principle of minimized free energy, this is the most stable state for Sys. A, as shown in Figure 6(a), occurring at $\phi_{oil}^{\alpha} = 0$. In this state, all oil molecules are homogeneously dissolved within the aqueous solution, aligning with the MD simulation (Figure 4(a)) and corresponding closely with the experimental observation (Figure 2(b)). For Sys. B, Figure 6(b) presents the free-energy curve where the minimum occurs for $0 < \phi_{oil}^{\alpha} < 1$. This minimum indicates a stable state in which oil molecules coexist across the droplet (α) and mixing solution (β) phases. This configuration matches well with both the MD simulation outcomes shown in Figure 4(b) and the experimental observations of SFMEs in Figure 2(b). In Sys. C, the lowest free energy point is found at $\phi_{oil}^{\alpha} = 1$, as illustrated in Figure 6(c). This suggests complete phase separation, where all oil molecules reside in the droplet phase. This theoretical approach not only substantiates the empirical observations but also provides a quantitative framework for understanding the energetics and phase behavior underlying the formation and stability of SFMEs.

In the MD studies, Sys. B typifies the surfactant-free microemulsion system, characterized by the presence of multiple stable nanodroplets. This system stands distinct from Systems A and C due to its unique phase behavior. In Sys. B, oil molecules are distributed between both the solution phase (β phase) and the droplet phase (α phase), facilitating coexistence. This suggests that Sys. B acts as a transitional regime between the homogeneous solution of Sys. A and the segregated phase of Sys. C. The mechanism underlying the coexistence of oil molecules in both phases within Sys. B can be elucidated in eq 4. The free energy $f(\phi_{oil}^{\alpha}, \phi_i)$ comprises two primary components: the initial three terms represent the mixing entropy, and the latter three terms account for the internal energy. The mixing entropy promotes the dissolution of oil molecules into the β phase, leading to a uniform molecular dispersion, as observed in Sys. A. Conversely, the internal energy favors the aggregation of oil molecules away from the solution, resulting in droplet formation as seen in Sys. C. The balance between these two forces dictates the distribution of oil molecules: dominance of mixing entropy results in a homogeneous solution, whereas prevalence of internal energy leads to phase separation.

In Sys. B, where the chemical potential is in equilibrium, oil molecules partition between the solution and droplet phases, achieving a stable coexistence. This equilibrium is influenced by the volume fractions ϕ_i and the interaction parameter χ_{ij}. High concentrations of a hydrotrope, such as ethanol (ϕ_e), enhance the mixing entropy, favoring the formation of homogeneous solutions. In contrast, the reduced ethanol content increases the internal energy, promoting phase separation. An intermediate ethanol content allows for

https://doi.org/10.1021/acs.langmuir.4c03761
Langmuir XXXX, XXX, XXX−XXX

balanced contributions from both mixing entropy and internal energy, resulting in the formation of a nanodroplet solution typical of SFMEs. Additionally, variations in water content directly impact ϕ_e, facilitating transitions among homogeneous solutions, coexistence, and phase separation, as altering water content modifies the solubilization dynamics of oil molecules. These theoretical insights are supported by a range of experimental findings.[21,57−60] Notably, the formation of the "ouze effect", a phenomenon similar to the transitions observed in our system, has been documented in the literature.[21] This alignment between theoretical predictions and empirical evidence underscores the validity of the extended H−F theory in explaining the stability and phase behavior of SFMEs, highlighting the complex interplay of the intermolecular potential energy and phase dynamics in these systems.

In the study of phase behavior within the water/ethanol/oil system, the theoretical constructs of spinodal and binodal lines provide critical insight into the transitions observed across different phase behaviors. We constructed a ternary phase diagram, as illustrated in Figure 6(d). The phase transitions can be systematically traced by varying the fractions of ethanol (ϕ_e) and water (ϕ_w), progressing from Sys. A, through Sys. B, to Sys. C.

In Figure 6(d), the critical point of the phase transition is identified where the spinodal and binodal lines intersect (with reference to eq 9 in ref 72). Above this critical point lies the single-phase region, while below it the system exhibits multiphase behaviors, encompassing both transition regions (such as the ouzo effect) and phase separation. The critical ethanol fraction, denoted as $\phi_{e,cri}$, represents the position of this critical point here. Generally, an increase in $\phi_{e,cri}$ expands the multiphase region, indicating a greater tendency for the system to transition from a single state to a multiphase state. To further understand the factors influencing $\phi_{e,cri}$, we consider the impact of the interaction parameter between water and oil, χ_{ow}, and temperature, T. The parameter χ_{ow} quantifies the internal energy arising from the mixing of water and oil; a higher χ_{ow} suggests greater internal energy, which discourages mixing due to the energy minimization principle and instead favors phase separation. Correspondingly, Figure 6(e) illustrates that as χ_{ow} increases, $\phi_{e,cri}$ also rises, enlarging the multiphase region and facilitating the formation of a multiphase system. This aligns with the theoretical expectations. Conversely, as the temperature T increases, $\phi_{e,cri}$ decreases, as depicted in Figure 6(f). This trend indicates a reduction in the multiphase region with rising temperature, which discourages phase separation. This temperature effect can be attributed to an increase in the entropy, which promotes mixing and favors the formation of a single-phase solution. These observations are consistent with our previous experimental findings,[59] reinforcing the understanding of temperature and interaction parameters as critical factors in phase behavior dynamics.

It should be noted, however, that while the results from both MD simulations and F−H theory exhibit a general correspondence, the theoretical model does incorporate simplifications that could limit its accuracy. The F−H theory traditionally simplifies interactions and molecular configurations, such as neglecting the effects of bond angles, bond rigidity, and overlapping volumes of spherical beads. These simplifications mean that while the MD and experimental results can be roughly aligned with theoretical predictions, achieving precise correspondence, e.g., for a specific ternary system, is challenging. Despite its current exclusion, the experimentally measured zeta potential is acknowledged as a critical factor in the colloidal stability of nanodroplets against coalescence. Future improvements in our model will focus on detailed charge interactions at the interface, inspired by the foundational work of Zemb et al.[21] and Rak et al.,[28,29] which highlights the role of the zeta potential in stabilizing mesoscale structures. This enhancement will be supported by advancements in all-atom MD simulations and refined theoretical approaches that better capture these dynamics.

Discussion. From the conducted studies, Sys. B, situated in the transitional zone, exhibits unique structural behavior compared to Systems C and A, which are in the multiphase and monophasic zones, respectively. Specifically, Sys. B forms stable nanodroplets on the mesoscopic scale and appears transparent on the macroscopic scale. This system, classified as a surfactant-free microemulsion, does not contain conventional surfactants. Instead, it contains mesoscopic nanodroplets that create numerous two-phase interfaces, offering broad applicability across various fields.[15] Unlike surfactant-based microemulsions (SBMEs), which consume less substance and stabilize nanodroplets by forming a flexible film at the oil−water interface with ultralow interfacial tension ($\gamma \approx 0$), SFMEs employ a hydrotrope distributed both at the interface and extensively in the continuous phase, as depicted in Figure 5. This distribution suggests that the stabilization of nanodroplets in SFMEs involves not only reducing interfacial tension but also other factors such as the differential solubility of ethanol in oil and water and mixing entropy. The effects of these factors, particularly solubility differences and ethanol content, warrant further detailed investigation.[57]

In our research, we examined the combined effects of mixing entropy and miscibility through the extended Flory−Huggins (F−H) theory, as described in eq 4. The results, illustrated in Figure 6, reveal that ethanol, acting as a hydrotrope in the ternary system of water/ethanol/oil, enhances the solubility of oil when present, mimicking the solubilizing impact typically seen with cosolvents. This effect hinges on the proportion of the ethanol and the interaction parameters between the components. Manipulation of the ethanol fraction ϕ_e allows for transitioning among the three phases: increasing ϕ_e or decreasing ϕ_w shifts the system from a multiphase to a single-phase zone, thus enhancing the entropy contribution to the free energy while reducing the internal energy influence and vice versa. Such insights enable practitioners to adjust ϕ_w, ϕ_e, and ϕ_o in practical applications to control the formation and dissolution of mesoscopic nanodroplets. Additionally, our study also sheds light on the mechanism of the "Ouze effect", which occurs with the addition of the traditional solvent "water". This corresponds to the transition from SFME to the phase separation. The reason is that water takes away the cohydrotrope (ethanol) that dissolves the oil and forces it to precipitate.

■ CONCLUSIONS

Surfactant-free microemulsions (SFMEs) are intriguing systems formed from ternary mixtures of two immiscible fluids—water and oil—and a hydrotrope, such as ethanol. The structures and properties of SFMEs bear similarities to those of surfactant-based microemulsions (SBMEs), particularly in terms of the enrichment of amphiphilic ethanol at the oil−water interface. Despite these similarities, the mechanisms stabilizing SFMEs differ significantly from those in SBMEs,

https://doi.org/10.1021/acs.langmuir.4c03761
Langmuir XXXX, XXX, XXX−XXX

marking a distinctive area of study within colloid and interface science.

In this work, we conducted an in-depth investigation of the spontaneous nucleation and stabilization mechanisms of SFMEs, employing experimental techniques, molecular dynamics (MD) simulations, and extended Flory−Huggins (F−H) theory. The formation of multiscale nanostructures (characteristic scales of ∼1 and ∼100 nm) and their interfacial charging characteristics in SFMEs have been clearly revealed experimentally. As the composition approaches the phase boundary, the magnitude of the zeta potential escalates, suggesting higher colloid stability. Moreover, these nanostructure populations transition from almost electrically neutral to strongly negative, a phenomenon that has been reported for the first time to the best of our knowledge. Based on MD simulation and classical nucleation theory, we found that nanodroplets can spontaneously nucleate in a certain ethanol−water mixture solution due to the higher supersaturation of oil molecules in the corresponding mixture solution and the lower interfacial tension. Our theoretical analysis also revealed that the stability of mesoscopic nanodroplets within SFMEs hinges on a delicate balance between the mixing entropy and internal energy. Specifically, when mixing entropy predominates, the system tends toward a homogeneous molecular solution characteristic of the single-phase zone. Conversely, dominance by internal energy leads to phase separation within the multiphase zone. When these two forces are comparable in magnitude, the system stabilizes into nanodroplet solutions, showcasing microscopically nanostructured environments. The dynamic transitions among these three phases can be manipulated by adjusting the volume fractions of the components and interaction parameters, demonstrating the tunability of SFMEs through compositional changes.

Although the extended Flory−Huggins theory provides a framework for understanding some of the phenomena observed in MD simulations and experimental setups, it remains clear that accurate quantitative predictions are challenging. Further refinement of this theoretical model is essential, possibly through integration of more precise MD simulations and thermodynamic analyses, such as the contribution of charges.

■ ASSOCIATED CONTENT

Supporting Information

The Supporting Information is available free of charge at https://pubs.acs.org/doi/10.1021/acs.langmuir.4c03761.

Measurements of viscosity, refractive index, and dielectric constant of ternary solutions with different compositions; parameters for the interaction between different molecules in molecular simulation; and calculation of the droplet nucleation barrier based on classical nucleation theory (ZIP)

■ AUTHOR INFORMATION

Corresponding Authors

Mingbo Li − *Key Laboratory of Hydrodynamics (Ministry of Education), School of Ocean and Civil Engineering, Shanghai Jiao Tong University, Shanghai 200240, China;* orcid.org/0009-0000-6692-0887; Email: mingboli@sjtu.edu.cn

Chao Sun − *New Cornerstone Science Laboratory, Center for Combustion Energy, Key Laboratory for Thermal Science and Power Engineering of Ministry of Education, Department of Energy and Power Engineering, Tsinghua University, Beijing 100084, China; Department of Engineering Mechanics, School of Aerospace Engineering, Tsinghua University, Beijing 100084, China;* orcid.org/0000-0002-0930-6343; Email: chaosun@tsinghua.edu.cn

Authors

Changsheng Chen − *New Cornerstone Science Laboratory, Center for Combustion Energy, Key Laboratory for Thermal Science and Power Engineering of Ministry of Education, Department of Energy and Power Engineering, Tsinghua University, Beijing 100084, China*

Yawen Gao − *New Cornerstone Science Laboratory, Center for Combustion Energy, Key Laboratory for Thermal Science and Power Engineering of Ministry of Education, Department of Energy and Power Engineering, Tsinghua University, Beijing 100084, China*

Complete contact information is available at: https://pubs.acs.org/10.1021/acs.langmuir.4c03761

Notes

The authors declare no competing financial interest.

■ ACKNOWLEDGMENTS

This work is supported by the National Natural Science Foundation of China under grants nos. 11988102, 12202244, and 52406254, the National Key R&D Program of China under grant no. 2021YFA0716201, the New Cornerstone Investigator Program, the Xplorer Prize, the Postdoctoral Fellowship Program of CPSF (no. GZC20231217), and the China Postdoctoral Science Foundation (no. 2024M751663).

■ REFERENCES

(1) Winsor, P. Hydrotropy, solubilisation and related emulsification processes. *Trans. Faraday Soc.* **1948**, *44*, 376−398.

(2) McClements, D. J. Nanoemulsions versus microemulsions: terminology, differences, and similarities. *Soft Matter* **2012**, *8*, 1719−1729.

(3) Fryd, M. M.; Mason, T. G. Advanced nanoemulsions. *Annu. Rev. Phys. Chem.* **2012**, *63*, 493−518.

(4) Gradzielski, M.; Duvail, M.; de Molina, P. M.; Simon, M.; Talmon, Y.; Zemb, T. Using microemulsions: formulation based on knowledge of their mesostructure. *Chem. Rev.* **2021**, *121*, 5671−5740.

(5) Bouchemal, K.; Briançon, S.; Perrier, E.; Fessi, H. Nano-emulsion formulation using spontaneous emulsification: solvent, oil and surfactant optimization. *Int. J. Pharm.* **2004**, *280*, 241−251.

(6) Srivastava, V. K.; Kini, G.; Rout, D. Detergency in spontaneously formed emulsions. *J. Colloid Interface Sci.* **2006**, *304*, 214−221.

(7) Anton, N.; Benoit, J.-P.; Saulnier, P. Design and production of nanoparticles formulated from nano-emulsion templates—A review. *J. Controlled Release* **2008**, *128*, 185−199.

(8) Gutiérrez, J.; González, C.; Maestro, A.; Solè, I.; Pey, C.; Nolla, J. Nano-emulsions: New applications and optimization of their preparation. *Curr. Opin. Colloid Interface Sci.* **2008**, *13*, 245−251.

(9) Lohse, D.; Zhang, X. Physicochemical hydrodynamics of droplets out of equilibrium. *Nat. Rev. Phys.* **2020**, *2*, 426−443.

(10) Moulik, S. P.; Paul, B. K. Structure, dynamics and transport properties of microemulsions. *Adv. Colloid Interface Sci.* **1998**, *78*, 99−195.

(11) Liu, D.; Huang, Z.; Suo, Y.; Zhu, P.; Tan, J.; Lu, H. CO2-Responsive Surfactant-Free Microemulsion. *Langmuir* **2018**, *34*, 8910−8916.

(12) Tanford, C. Micelle shape and size. *J. Phys. Chem.* **1972**, *76*, 3020−3024.

(13) Subramanian, D.; Boughter, C. T.; Klauda, J. B.; Hammouda, B.; Anisimov, M. A. Mesoscale inhomogeneities in aqueous solutions of small amphiphilic molecules. *Faraday Discuss.* **2014**, *167*, 217−238.
(14) Schoettl, S.; Marcus, J.; Diat, O.; Touraud, D.; Kunz, W.; Zemb, T.; Horinek, D. Emergence of surfactant-free micelles from ternary solutions. *Chem. Sci.* **2014**, *5*, 2949−2954.
(15) Hou, W.; Xu, J. Surfactant-free microemulsions. *Curr. Opin. Colloid Interface Sci.* **2016**, *25*, 67−74.
(16) Hodgdon, T. K.; Kaler, E. W. Hydrotropic solutions. *Curr. Opin. Colloid Interface Sci.* **2007**, *12*, 121−128.
(17) Xu, J.; Yin, A.; Zhao, J.; Li, D.; Hou, W. Surfactant-free microemulsion composed of oleic acid, n-propanol, and H2O. *J. Phys. Chem. B* **2013**, *117*, 450−456.
(18) Novikov, A. A.; Semenov, A. P.; Kuchierskaya, A. A.; Kopitsyn, D. S.; Vinokurov, V. A.; Anisimov, M. A. Generic nature of interfacial phenomena in solutions of nonionic hydrotropes. *Langmuir* **2019**, *35*, 13480−13487.
(19) Smith, G. D.; Donelan, C. E.; Barden, R. E. Oil-continuous microemulsions composed of hexane, water, and 2-propanol. *J. Colloid Interface Sci.* **1977**, *60*, 488−496.
(20) Kunz, W.; Holmberg, K.; Zemb, T. Hydrotropes. *Curr. Opin. Colloid Interface Sci.* **2016**, *22*, 99−107.
(21) Zemb, T. N.; Klossek, M.; Lopian, T.; Marcus, J.; Schoettl, S.; Horinek, D.; Prevost, S. F.; Touraud, D.; Diat, O.; Marcelja, S.; Kunz, W. How to explain microemulsions formed by solvent mixtures without conventional surfactants. *Proc. Natl. Acad. Sci. U. S. A.* **2016**, *113*, 4260−4265.
(22) Keiser, B. A.; Varie, D.; Barden, R. E.; Holt, S. L. Detergentless water/oil microemulsions composed of hexane, water, and 2-propanol. 2. Nuclear magnetic resonance studies, effect of added sodium chloride. *J. Phys. Chem.* **1979**, *83*, 1276−1280.
(23) Khmelnitsky, Y. L.; Van Hoek, A.; Veeger, C.; Visser, A. J. Detergentless microemulsions as media for enzymatic reactions: spectroscopic and ultracentrifugation studies. *J. Phys. Chem.* **1989**, *93*, 872−878.
(24) Klossek, M. L.; Touraud, D.; Zemb, T.; Kunz, W. Structure and solubility in surfactant-free microemulsions. *ChemPhysChem* **2012**, *13*, 4116−4119.
(25) Xu, J.; Song, J.; Deng, H.; Hou, W. Surfactant-free microemulsions of 1-butyl-3-methylimidazolium hexafluorophosphate, diethylammonium formate, and water. *Langmuir* **2018**, *34*, 7776−7783.
(26) Prevost, S.; Lopian, T.; Pleines, M.; Diat, O.; Zemb, T. Small-angle scattering and morphologies of ultra-flexible microemulsions. *J. Appl. Crystallogr.* **2016**, *49*, 2063−2072.
(27) Robertson, A. E.; Phan, D. H.; Macaluso, J. E.; Kuryakov, V. N.; Jouravleva, E. V.; Bertrand, C. E.; Yudin, I. K.; Anisimov, M. A. Mesoscale solubilization and critical phenomena in binary and quasi-binary solutions of hydrotropes. *Fluid Phase Equilib.* **2016**, *407*, 243−254.
(28) Rak, D.; Sedlák, M. On the mesoscale solubility in liquid solutions and mixtures. *J. Phys. Chem. B* **2019**, *123*, 1365−1374.
(29) Rak, D.; Sedlák, M. Solvophobicity-driven mesoscale structures: stabilizer-free nanodispersions. *Langmuir* **2023**, *39*, 1515−1528.
(30) Novikov, A. A.; Semenov, A. P.; Monje-Galvan, V.; Kuryakov, V. N.; Klauda, J. B.; Anisimov, M. A. Dual action of hydrotropes at the water/oil interface. *J. Phys. Chem. C* **2017**, *121*, 16423−16431.
(31) Nannette, C.; Baudry, J.; Chen, A.; Song, Y.; Shglabow, A.; Bremond, N.; Démoulin, D.; Walters, J.; Weitz, D. A.; Bibette, J. Thin adhesive oil films lead to anomalously stable mixtures of water in oil. *Science* **2024**, *384*, 209−213.
(32) Pullanchery, S.; Kulik, S.; Rehl, B.; Hassanali, A.; Roke, S. Charge transfer across C− H···O hydrogen bonds stabilizes oil droplets in water. *Science* **2021**, *374*, 1366−1370.
(33) Ma, J.; Yao, M.; Yang, Y.; Zhang, X. Comprehensive review on stability and demulsification of unconventional heavy oil-water emulsions. *J. Mol. Liq.* **2022**, *350*, 118510.
(34) Vitale, S. A.; Katz, J. L. Liquid droplet dispersions formed by homogeneous liquid- liquid nucleation:"The ouzo effect. *Langmuir* **2003**, *19*, 4105−4110.
(35) Wang, Y.-R.; Duan, L.-L.; Cheng, S.-Q.; Chai, B.; Han, F. Water/i-Propanol/n-Butanol Microemulsions. *J. Dispersion Sci. Technol.* **2008**, *29*, 280−283.
(36) Ni, P.; HOU, W.-G. A Novel Surfactant-free Microemulsion System: Ethanol/Furaldehyde/H2O. *Chin. J. Chem.* **2008**, *26*, 1985−1990.
(37) Xu, J.; Zhang, L.; Yin, A.; Hou, W.; Yang, Y. Nonaqueous ionic liquid microemulsions of 1-butyl-3-methylimidazolium tetrafluoroborate, toluene and ethanol. *Soft Matter* **2013**, *9*, 6497−6504.
(38) Xu, J.; Zhang, L.; Li, C.; Zhan, T.; Hou, W. Ionic liquid microemulsions of 1-butyl-3-methylimidazolium hexafluorophosphate, N, N-dimethylformamide, and water. *RSC Adv.* **2013**, *3*, 21494−21500.
(39) Bošković, P.; Sokol, V.; Zemb, T.; Touraud, D.; Kunz, W. Weak micelle-like aggregation in ternary liquid mixtures as revealed by conductivity, surface tension, and light scattering. *J. Phys. Chem. B* **2015**, *119*, 9933−9939.
(40) Kamogawa, K.; Matsumoto, M.; Kobayashi, T.; Sakai, T.; Sakai, H.; Abe, M. Dispersion and stabilizing effects of n-hexadecane on tetralin and benzene metastable droplets in surfactant-free conditions. *Langmuir* **1999**, *15*, 1913−1917.
(41) Sakai, T. Surfactant-free emulsions. *Curr. Opin. Colloid Interface Sci.* **2008**, *13*, 228−235.
(42) Creux, P.; Lachaise, J.; Graciaa, A.; Beattie, J. K.; Djerdjev, A. M. Strong Specific Hydroxide Ion Binding at the Pristine Oil/Water and Air/Water Interfaces. *J. Phys. Chem. B* **2009**, *113*, 14146−14150.
(43) Roger, K.; Cabane, B. Why are hydrophobic/water interfaces negatively charged? *Angew. Chem., Int. Ed.* **2012**, *51*, 5625.
(44) Jena, K. C.; Scheu, R.; Roke, S. Surface impurities are not responsible for the charge on the oil/water interface: a comment. *Angew. Chem., Int. Ed.* **2012**, *51*, 12938−12940.
(45) Lu, Z.; Schaarsberg, M. H. K.; Zhu, X.; Yeo, L. Y.; Lohse, D.; Zhang, X. Universal nanodroplet branches from confining the Ouzo effect. *Proc. Natl. Acad. Sci. U. S. A.* **2017**, *114*, 10332−10337.
(46) Xenakis, A.; Zoumpanioti, M.; Stamatis, H. Enzymatic reactions in structured surfactant-free microemulsions. *Curr. Opin. Colloid Interface Sci.* **2016**, *22*, 41−45.
(47) Krickl, S.; Touraud, D.; Bauduin, P.; Zinn, T.; Kunz, W. Enzyme activity of horseradish peroxidase in surfactant-free microemulsions. *J. Colloid Interface Sci.* **2018**, *516*, 466−475.
(48) Xu, J.; Deng, H.; Song, J.; Zhao, J.; Zhang, L.; Hou, W. Synthesis of hierarchical flower-like Mg2Al-Cl layered double hydroxide in a surfactant-free reverse microemulsion. *J. Colloid Interface Sci.* **2017**, *505*, 816−823.
(49) Song, L.; Jia, H.; Zhang, F.; Jia, H.; Wang, Y.; Xie, Q.; Fan, F.; Wang, Q.; Wen, S. Sustainable Utilization of Surfactant-Free Microemulsion Regulated by CO2 for Treating Oily Wastes: A Interpretation of the Response Mechanism. *Langmuir* **2024**, *40*, 960−967.
(50) Degot, P.; Huber, V.; Hofmann, E.; Hahn, M.; Touraud, D.; Kunz, W. Solubilization and extraction of curcumin from Curcuma Longa using green, sustainable, and food-approved surfactant-free microemulsions. *Food Chem.* **2021**, *336*, 127660.
(51) Xu, J.; Zhang, L.; Li, D.; Zhao, J.; Hou, W. Synthesis of Mg 2 Al-Cl layered double hydroxide nanosheets in a surfactant-free reverse microemulsion. *Colloid Polym. Sci.* **2013**, *291*, 2515−2521.
(52) Zhan, T.; Zhang, Y.; Yang, Q.; Deng, H.; Xu, J.; Hou, W. Ultrathin layered double hydroxide nanosheets prepared from a water-in-ionic liquid surfactant-free microemulsion for phosphate removal from aquatic systems. *Chem. Eng. J.* **2016**, *302*, 459−465.
(53) Mirhoseini, B. S.; Salabat, A. A novel surfactant-free microemulsion system for the synthesis of poly (methyl methacrylate)/Ag nanocomposite. *J. Mol. Liq.* **2021**, *342*, 117555.
(54) Wolf, S.; Feldmann, C. Microemulsions: Options to expand the synthesis of inorganic nanoparticles. *Angew. Chem., Int. Ed.* **2016**, *55*, 15728−15752.

https://doi.org/10.1021/acs.langmuir.4c03761
Langmuir XXXX, XXX, XXX−XXX

(55) Cui, X.; Wang, J.; Zhang, X.; Wang, Q.; Song, M.; Chai, J. Preparation of Nano-TiO2 by a surfactant-free microemulsion−hydrothermal method and its photocatalytic activity. *Langmuir* **2019**, *35*, 9255−9263.
(56) Du, A. W.; Stenzel, M. H. Drug carriers for the delivery of therapeutic peptides. *Biomacromolecules* **2014**, *15*, 1097−1114.
(57) Han, Y.; Pan, N.; Li, D.; Liu, S.; Sun, B.; Chai, J.; Li, D. Formation mechanism of surfactant-free microemulsion and a judgment on whether it can be formed in one ternary system. *Chem. Eng. J.* **2022**, *437*, 135385.
(58) Li, M.; Yi, L.; Sun, C. Spontaneously formed multiscale nanodomains in monophasic region of ternary solution. *J. Colloid Interface Sci.* **2022**, *628*, 223−235.
(59) Li, M.; Wakata, Y.; Zeng, H.; Sun, C. On the thermal response of multiscale nanodomains formed in trans-anethol/ethanol/water surfactant-free microemulsion. *J. Colloid Interface Sci.* **2023**, *652*, 1944−1953.
(60) Liu, Y.; Xu, J.; Deng, H.; Song, J.; Hou, W. A surfactant-free microemulsion composed of isopentyl acetate, n-propanol, and water. *RSC Adv.* **2018**, *8*, 1371−1377.
(61) Ma, X.; Li, M.; Sun, C. Measurement and characterization of bulk nanobubbles by nanoparticle tracking analysis method. *J. Hydrodyn.* **2022**, *34*, 1121−1133.
(62) Plimpton, S. Fast parallel algorithms for short-range molecular dynamics. *J. Comput. Phys.* **1995**, *117*, 1−19.
(63) Warner, Jr. H. R. Kinetic theory and rheology of dilute suspensions of finitely extendible dumbbells. *Ind. Eng. Chem. Fundam.* **1972**, *11*, 379−387.
(64) Flory, P. J. Thermodynamics of high polymer solutions. *J. Phys. Chem.* **1942**, *10*, 51−61.
(65) Huggins, M. L. Some properties of solutions of long-chain compounds. *J. Phys. Chem.* **1942**, *46*, 151−158.
(66) Flory, P. J. *Principles of Polymer Chemistry*; Cornell University Press, 1953.
(67) Doi, M. *Soft Matter Physics*; Oxford University Press, 2013.
(68) Dudowicz, J.; Freed, K. F.; Douglas, J. F. Communication: Cosolvency and cononsolvency explained in terms of a Flory-Huggins type theory. *J. Chem. Phys.* **2015**, *143*, 131101.
(69) Kim, J. Y. Phase diagrams of ternary π-conjugated polymer solutions for organic photovoltaics. *Polymers* **2021**, *13*, 983.
(70) Sato, T.; Takahashi, R. Competition between the micellization and the liquid−liquid phase separation in amphiphilic block copolymer solutions. *Polym. J.* **2017**, *49*, 273−277.
(71) Mukherji, D.; Marques, C. M.; Kremer, K. Smart responsive polymers: Fundamentals and design principles. *Annu. Rev. Condens. Matter Phys.* **2020**, *11*, 271−299.
(72) Shcherbakova, N.; Gerbaud, V.; Roger, K. Using the Intrinsic Geometry of Binodal Curves to Simplify the Computation of Ternary Liquid−Liquid Phase Diagrams. *Entropy* **2023**, *25*, 1329.

https://doi.org/10.1021/acs.langmuir.4c03761
Langmuir XXXX, XXX, XXX−XXX